Biomedical Optics EXPRESS

Adaptive optics retinal imaging in the living mouse eye

Ying Geng,[1,2,*] Alfredo Dubra,[1,3,4] Lu Yin,[1] William H. Merigan,[1,3] Robin Sharma,[1,2] Richard T. Libby,[1,3] and David R. Williams[1,2,3]

[1]*Center for Visual Science, University of Rochester, Rochester, NY 14627, USA*
[2]*The Institute of Optics, University of Rochester, Rochester, NY 14620, USA*
[3]*Flaum Eye Institute, University of Rochester, Rochester, NY 14642, USA*
[4]*Current address: Eye Institute, Medical College of Wisconsin, WI 53226, USA*
**gengy@corning.com*

Abstract: Correction of the eye's monochromatic aberrations using adaptive optics (AO) can improve the resolution of *in vivo* mouse retinal images [Biss et al., Opt. Lett. **32**(6), 659 (2007) and Alt et al., Proc. SPIE **7550**, 755019 (2010)], but previous attempts have been limited by poor spot quality in the Shack-Hartmann wavefront sensor (SHWS). Recent advances in mouse eye wavefront sensing using an adjustable focus beacon with an annular beam profile have improved the wavefront sensor spot quality [Geng et al., Biomed. Opt. Express **2**(4), 717 (2011)], and we have incorporated them into a fluorescence adaptive optics scanning laser ophthalmoscope (AOSLO). The performance of the instrument was tested on the living mouse eye, and images of multiple retinal structures, including the photoreceptor mosaic, nerve fiber bundles, fine capillaries and fluorescently labeled ganglion cells were obtained. The *in vivo* transverse and axial resolutions of the fluorescence channel of the AOSLO were estimated from the full width half maximum (FWHM) of the line and point spread functions (LSF and PSF), and were found to be better than 0.79 μm ± 0.03 μm (STD)(45% wider than the diffraction limit) and 10.8 μm ± 0.7 μm (STD)(two times the diffraction limit), respectively. The axial positional accuracy was estimated to be 0.36 μm. This resolution and positional accuracy has allowed us to classify many ganglion cell types, such as bistratified ganglion cells, *in vivo*.

© 2012 Optical Society of America

OCIS codes: (170.4460) Ophthalmic optics and devices; (110.1080) Active or adaptive optics; (330.7324) Visual optics, comparative animal models.

References

1. G. J. Chader, "Animal models in research on retinal degenerations: past progress and future hope," Vision Res. **42**(4), 393–399 (2002).
2. H. Levkovitch-Verbin, "Animal models of optic nerve diseases," Eye (Lond.) **18**(11), 1066–1074 (2004).
3. R. T. Libby, M. G. Anderson, I. H. Pang, Z. H. Robinson, O. V. Savinova, I. M. Cosma, A. Snow, L. A. Wilson, R. S. Smith, A. F. Clark, and S. W. John, "Inherited glaucoma in DBA/2J mice: pertinent disease features for studying the neurodegeneration," Vis. Neurosci. **22**(05), 637–648 (2005).
4. B. Chang, N. L. Hawes, R. E. Hurd, J. Wang, D. Howell, M. T. Davisson, T. H. Roderick, S. Nusinowitz, and J. R. Heckenlively, "Mouse models of ocular diseases," Vis. Neurosci. **22**(05), 587–593 (2005).
5. M. W. Seeliger, S. C. Beck, N. Pereyra-Muñoz, S. Dangel, J. Y. Tsai, U. F. Luhmann, S. A. van de Pavert, J. Wijnholds, M. Samardzija, A. Wenzel, E. Zrenner, K. Narfström, E. Fahl, N. Tanimoto, N. Acar, and F. Tonagel, "*In vivo* confocal imaging of the retina in animal models using scanning laser ophthalmoscopy," Vision Res. **45**(28), 3512–3519 (2005).
6. V. J. Srinivasan, T. H. Ko, M. Wojtkowski, M. Carvalho, A. Clermont, S. E. Bursell, Q. H. Song, J. Lem, J. S. Duker, J. S. Schuman, and J. G. Fujimoto, "Noninvasive volumetric imaging and morphometry of the rodent retina with high-speed, ultrahigh-resolution optical coherence tomography," Invest. Ophthalmol. Vis. Sci. **47**(12), 5522–5528 (2006).

#160500 - $15.00 USD Received 3 Jan 2012; revised 13 Feb 2012; accepted 14 Feb 2012; published 15 Mar 2012
(C) 2012 OSA

7. M. Paques, M. Simonutti, M. J. Roux, S. Picaud, E. Levavasseur, C. Bellman, and J.-A. Sahel, "High resolution fundus imaging by confocal scanning laser ophthalmoscopy in the mouse," Vision Res. **46**(8-9), 1336–1345 (2006).
8. M. Ruggeri, H. Wehbe, S. Jiao, G. Gregori, M. E. Jockovich, A. Hackam, Y. Duan, and C. A. Puliafito, "*In vivo* three-dimensional high-resolution imaging of rodent retina with spectral-domain optical coherence tomography," Invest. Ophthalmol. Vis. Sci. **48**(4), 1808–1814 (2007).
9. A. Maass, P. L. von Leithner, V. Luong, L. Guo, T. E. Salt, F. W. Fitzke, and M. F. Cordeiro, "Assessment of rat and mouse RGC apoptosis imaging *in vivo* with different scanning laser ophthalmoscopes," Curr. Eye Res. **32**(10), 851–861 (2007).
10. O. P. Kocaoglu, S. R. Uhlhorn, E. Hernandez, R. A. Juarez, R. Will, J. M. Parel, and F. Manns, "Simultaneous fundus imaging and optical coherence tomography of the mouse retina," Invest. Ophthalmol. Vis. Sci. **48**(3), 1283–1289 (2007).
11. H. Murata, M. Aihara, Y. N. Chen, T. Ota, J. Numaga, and M. Araie, "Imaging mouse retinal ganglion cells and their loss *in vivo* by a fundus camera in the normal and ischemia-reperfusion model," Invest. Ophthalmol. Vis. Sci. **49**(12), 5546–5552 (2008).
12. M. K. Walsh and H. A. Quigley, "*In vivo* time-lapse fluorescence imaging of individual retinal ganglion cells in mice," J. Neurosci. Methods **169**(1), 214–221 (2008).
13. M. D. Fischer, G. Huber, S. C. Beck, N. Tanimoto, R. Muehlfriedel, E. Fahl, C. Grimm, A. Wenzel, C. E. Remé, S. A. van de Pavert, J. Wijnholds, M. Pacal, R. Bremner, and M. W. Seeliger, "Noninvasive, *in vivo* assessment of mouse retinal structure using optical coherence tomography," PLoS ONE **4**(10), e7507 (2009).
14. C. K. S. Leung, R. N. Weinreb, Z. W. Li, S. Liu, J. D. Lindsey, N. Choi, L. Liu, C. Y. L. Cheung, C. Ye, K. L. Qiu, L. J. Chen, W. H. Yung, J. G. Crowston, M. L. Pu, K. F. So, C. P. Pang, and D. S. C. Lam, "Long-term *in vivo* imaging and measurement of dendritic shrinkage of retinal ganglion cells," Invest. Ophthalmol. Vis. Sci. **52**(3), 1539–1547 (2011).
15. Y. Geng, L. A. Schery, R. Sharma, A. Dubra, K. Ahmad, R. T. Libby, and D. R. Williams, "Optical properties of the mouse eye," Biomed. Opt. Express **2**(4), 717–738 (2011).
16. E. G. de la Cera, G. Rodríguez, L. Llorente, F. Schaeffel, and S. Marcos, "Optical aberrations in the mouse eye," Vision Res. **46**(16), 2546–2553 (2006).
17. J. Liang, D. R. Williams, and D. T. Miller, "Supernormal vision and high-resolution retinal imaging through adaptive optics," J. Opt. Soc. Am. A **14**(11), 2884–2892 (1997).
18. D. C. Gray, W. Merigan, J. I. Wolfing, B. P. Gee, J. Porter, A. Dubra, T. H. Twietmeyer, K. Ahamd, R. Tumbar, F. Reinholz, and D. R. Williams, "*In vivo* fluorescence imaging of primate retinal ganglion cells and retinal pigment epithelial cells," Opt. Express **14**(16), 7144–7158 (2006).
19. D. C. Gray, R. Wolfe, B. P. Gee, D. Scoles, Y. Geng, B. D. Masella, A. Dubra, S. Luque, D. R. Williams, and W. H. Merigan, "*In vivo* imaging of the fine structure of rhodamine-labeled macaque retinal ganglion cells," Invest. Ophthalmol. Vis. Sci. **49**(1), 467–473 (2008).
20. J. I. Morgan, A. Dubra, R. Wolfe, W. H. Merigan, and D. R. Williams, "*In vivo* autofluorescence imaging of the human and macaque retinal pigment epithelial cell mosaic," Invest. Ophthalmol. Vis. Sci. **50**(3), 1350–1359 (2009).
21. A. Dubra and Y. Sulai, "Reflective afocal broadband adaptive optics scanning ophthalmoscope," Biomed. Opt. Express **2**(6), 1757–1768 (2011).
22. A. Dubra, Y. Sulai, J. L. Norris, R. F. Cooper, A. M. Dubis, D. R. Williams, and J. Carroll, "Noninvasive imaging of the human rod photoreceptor mosaic using a confocal adaptive optics scanning ophthalmoscope," Biomed. Opt. Express **2**(7), 1864–1876 (2011).
23. D. P. Biss, D. Sumorok, S. A. Burns, R. H. Webb, Y. Zhou, T. G. Bifano, D. Côté, I. Veilleux, P. Zamiri, and C. P. Lin, "*In vivo* fluorescent imaging of the mouse retina using adaptive optics," Opt. Lett. **32**(6), 659–661 (2007).
24. C. Alt, D. P. Biss, N. Tajouri, T. C. Jakobs, and C. P. Lin, "An adaptive-optics scanning laser ophthalmoscope for imaging murine retinal microstructure," Proc. SPIE **7550**, 755019 (2010).
25. Y. Geng, K. P. Greenberg, R. Wolfe, D. C. Gray, J. J. Hunter, A. Dubra, J. G. Flannery, D. R. Williams, and J. Porter, "*In vivo* imaging of microscopic structures in the rat retina," Invest. Ophthalmol. Vis. Sci. **50**(12), 5872–5879 (2009).
26. A. Sorsby, M. Sheridan, G. A. Leary, and B. Benjamin, "Vision, visual acuity, and ocular refraction of young men: findings in a sample of 1,033 subjects," BMJ **1**(5183), 1394–1398 (1960).
27. Q. Wang, B. E. Klein, R. Klein, and S. E. Moss, "Refractive status in the Beaver Dam Eye Study," Invest. Ophthalmol. Vis. Sci. **35**(13), 4344–4347 (1994).
28. C. Schmucker and F. Schaeffel, "A paraxial schematic eye model for the growing C57BL/6 mouse," Vision Res. **44**(16), 1857–1867 (2004).
29. J. Tejedor and P. de la Villa, "Refractive changes induced by form deprivation in the mouse eye," Invest. Ophthalmol. Vis. Sci. **44**(1), 32–36 (2003).
30. Y. Le Grand, *Physiological Optics*, Vol. 13 of Springer Series in Optical Sciences (Springer-Verlag, Berlin, 1980), p. xvii.
31. A. Gómez-Vieyra, A. Dubra, D. Malacara-Hernández, and D. R. Williams, "First-order design of off-axis reflective ophthalmic adaptive optics systems using afocal telescopes," Opt. Express **17**(21), 18906–18919 (2009).

#160500 - $15.00 USD Received 3 Jan 2012; revised 13 Feb 2012; accepted 14 Feb 2012; published 15 Mar 2012
(C) 2012 OSA

32. G. Feng, R. H. Mellor, M. Bernstein, C. Keller-Peck, Q. T. Nguyen, M. Wallace, J. M. Nerbonne, J. W. Lichtman, and J. R. Sanes, "Imaging neuronal subsets in transgenic mice expressing multiple spectral variants of GFP," Neuron **28**(1), 41–51 (2000).
33. ANSI, "American National Standard for the Safe Use of Lasers ANSI Z136.1-2007" (Laser Institute of America, 2007).
34. F. C. Delori, R. H. Webb, and D. H. Sliney, American National Standards Institute, "Maximum permissible exposures for ocular safety (ANSI 2000), with emphasis on ophthalmic devices," J. Opt. Soc. Am. A **24**(5), 1250–1265 (2007).
35. A. Dubra and Z. Harvey, "Registration of 2D images from fast scanning ophthalmic instruments," in *Biomedical Image Registration*, B. Fischer, B. Dawant, and C. Lorenz, eds. (Springer Berlin, 2010), pp. 60–71.
36. L. Wang, J. Dong, G. Cull, B. Fortune, and G. A. Cioffi, "Varicosities of intraretinal ganglion cell axons in human and nonhuman primates," Invest. Ophthalmol. Vis. Sci. **44**(1), 2–9 (2003).
37. R. A. Cuthbertson and T. E. Mandel, "Anatomy of the mouse retina. Endothelial cell-pericyte ratio and capillary distribution," Invest. Ophthalmol. Vis. Sci. **27**(11), 1659–1664 (1986).
38. M. Paques, R. Tadayoni, R. Sercombe, P. Laurent, O. Genevois, A. Gaudric, and E. Vicaut, "Structural and hemodynamic analysis of the mouse retinal microcirculation," Invest. Ophthalmol. Vis. Sci. **44**(11), 4960–4967 (2003).
39. S. A. Burns, Z. Zhangyi, T. Y. P. Chui, H. Song, A. E. Elsner, and V. E. Malinovsky, "Imaging the inner retina using adaptive optics," nvest. Ophthalmol. Vis. Sci. **49**, 4512–9999 (2008).
40. J. Tam, J. A. Martin, and A. Roorda, "Noninvasive visualization and analysis of parafoveal capillaries in humans," Invest. Ophthalmol. Vis. Sci. **51**(3), 1691–1698 (2010).
41. C. J. Jeon, E. Strettoi, and R. H. Masland, "The major cell populations of the mouse retina," J. Neurosci. **18**(21), 8936–8946 (1998).
42. J. B. Schallek, B. D. Masella, J. J. Hunter, and D. R. Williams, "Stimulus-dependent Changes in capillary blood velocity revealed with adaptive optics scanning laser ophthalmoscopy," presented at The Association for Research in Vision and Ophthalmology Annual Meeting, Fort Lauderdale, FL, May 1–5, 2011).
43. Z. Y. Zhong, B. L. Petrig, X. F. Qi, and S. A. Burns, "*In vivo* measurement of erythrocyte velocity and retinal blood flow using adaptive optics scanning laser ophthalmoscopy," Opt. Express **16**(17), 12746–12756 (2008).
44. J. Tam, P. Tiruveedhula, and A. Roorda, "Characterization of single-file flow through human retinal parafoveal capillaries using an adaptive optics scanning laser ophthalmoscope," Biomed. Opt. Express **2**(4), 781–793 (2011).
45. Z. Y. Zhong, H. X. Song, T. Y. P. Chui, B. L. Petrig, and S. A. Burns, "Noninvasive measurements and analysis of blood velocity profiles in human retinal vessels," Invest. Ophthalmol. Vis. Sci. **52**(7), 4151–4157 (2011).
46. S. Thanos, L. Indorf, and R. Naskar, "*In vivo* FM: using conventional fluorescence microscopy to monitor retinal neuronal death *in vivo*," Trends Neurosci. **25**(9), 441–444 (2002).
47. T. Higashide, I. Kawaguchi, S. Ohkubo, H. Takeda, and K. Sugiyama, "*In vivo* imaging and counting of rat retinal ganglion cells using a scanning laser ophthalmoscope," Invest. Ophthalmol. Vis. Sci. **47**(7), 2943–2950 (2006).
48. J. Coombs, D. van der List, G. Y. Wang, and L. M. Chalupa, "Morphological properties of mouse retinal ganglion cells," Neuroscience **140**(1), 123–136 (2006).
49. W. Sun, N. Li, and S. He, "Large-scale morphological survey of mouse retinal ganglion cells," J. Comp. Neurol. **451**(2), 115–126 (2002).
50. T. C. Badea and J. Nathans, "Quantitative analysis of neuronal morphologies in the mouse retina visualized by using a genetically directed reporter," J. Comp. Neurol. **480**(4), 331–351 (2004).
51. J.-H. Kong, D. R. Fish, R. L. Rockhill, and R. H. Masland, "Diversity of ganglion cells in the mouse retina: unsupervised morphological classification and its limits," J. Comp. Neurol. **489**(3), 293–310 (2005).
52. S. Haverkamp and H. Wässle, "Immunocytochemical analysis of the mouse retina," J. Comp. Neurol. **424**(1), 1–23 (2000).
53. F. Chan, A. Bradley, T. G. Wensel, and J. H. Wilson, "Knock-in human rhodopsin-GFP fusions as mouse models for human disease and targets for gene therapy," Proc. Natl. Acad. Sci. U.S.A. **101**(24), 9109–9114 (2004).
54. A. Dhingra, P. Sulaiman, Y. Xu, M. E. Fina, R. W. Veh, and N. Vardi, "Probing neurochemical structure and function of retinal ON bipolar cells with a transgenic mouse," J. Comp. Neurol. **510**(5), 484–496 (2008).
55. J. G. Flannery, S. Zolotukhin, M. I. Vaquero, M. M. LaVail, N. Muzyczka, and W. W. Hauswirth, "Efficient photoreceptor-targeted gene expression *in vivo* by recombinant adeno-associated virus," Proc. Natl. Acad. Sci. U.S.A. **94**(13), 6916–6921 (1997).
56. F. Rolling, "Recombinant AAV-mediated gene transfer to the retina: gene therapy perspectives," Gene Ther. **11**(Suppl 1), S26–S32 (2004).
57. K. P. Greenberg, E. S. Lee, D. V. Schaffer, and J. G. Flannery, "Gene delivery to the retina using lentiviral vectors," Adv. Exp. Med. Biol. **572**, 255–266 (2006).
58. K. P. Greenberg, S. F. Geller, D. V. Schaffer, and J. G. Flannery, "Targeted transgene expression in muller glia of normal and diseased retinas using lentiviral vectors," Invest. Ophthalmol. Vis. Sci. **48**(4), 1844–1852 (2007).
59. P. Charbel Issa, M. S. Singh, D. M. Lipinski, N. V. Chong, F. C. Delori, A. R. Barnard, and R. E. Maclaren, "Optimization of *in vivo* confocal autofluorescence imaging of the ocular fundus in mice and its application to models of human retinal degeneration," Invest. Ophthalmol. Vis. Sci. **53**, iovs.11-8767 (2011).

#160500 - $15.00 USD Received 3 Jan 2012; revised 13 Feb 2012; accepted 14 Feb 2012; published 15 Mar 2012
(C) 2012 OSA

60. L. Yin, A. H. Cetin, Y. Geng, R. Sharma, A. Ahmad, E. M. Callaway, D. R. Williams, and W. H. Merigan, "*In vivo* optical recording from mouse retinal ganglion cells," presented at Neuroscience 2011, Society for Neuroscience Annual Meeting, Washington, DC, Nov. 12–16, 2011.
61. J. B. Schallek, Y. Geng, and D. R. Williams, "*In vivo* fluorescence adaptive optics scanning laser ophthalmoscopy (FAOSLO) of retinal pericytes and capillary blood flow in mice," to be presented at The Association for Research in Vision and Ophthalmology Annual Meeting, Fort Lauderdale, FL, May 6–10, 2012.
62. I. J. Kim, Y. F. Zhang, M. Meister, and J. R. Sanes, "Laminar restriction of retinal ganglion cell dendrites and axons: subtype-specific developmental patterns revealed with transgenic markers," J. Neurosci. **30**(4), 1452–1462 (2010).
63. Y. Han and S. C. Massey, "Electrical synapses in retinal ON cone bipolar cells: subtype-specific expression of connexins," Proc. Natl. Acad. Sci. U.S.A. **102**(37), 13313–13318 (2005).
64. W. Denk, J. H. Strickler, and W. W. Webb, "Two-photon laser scanning fluorescence microscopy," Science **248**(4951), 73–76 (1990).
65. J. J. Hunter, B. Masella, A. Dubra, R. Sharma, L. Yin, W. H. Merigan, G. Palczewska, K. Palczewski, and D. R. Williams, "Images of photoreceptors in living primate eyes using adaptive optics two-photon ophthalmoscopy," Biomed. Opt. Express **2**(1), 139–148 (2011).
66. R. Sharma, Y. Geng, L. Yin, W. H. Merigan, D. R. Williams, and J. J. Hunter, "*In vivo* two-photon imaging of mouse retina," to be presented at The Association for Research in Vision and Ophthalmology Annual Meeting, Fort Lauderdale, FL, May 6–10, 2012.

1. Introduction

Mouse models have become increasingly important for understanding the normal and diseased eye due to their availability for genetic manipulations not yet common in other mammals [1–4]. The conventional methods for studying mouse eye models are *in vitro* physiology and histology, which require a large number of animals for statistical analysis and do not allow for longitudinal studies in single animals. Non-invasive microscopic imaging of the mouse retina would allow tracking of retinal development, disease progression, or the efficacy of therapy in single animals over time. This can reduce the number of animals required and the animal-to-animal variability inherent in studying the dynamics of a process from different animals sacrificed at different time points. Recently, there have been a growing number of studies focused on *in vivo* optical imaging of the mouse retina, utilizing fundus cameras, scanning laser ophthalmoscopes (SLO), or optical coherence tomography (OCT) [5–14]. However, *in vivo* imaging resolution is compromised by ocular aberrations in the mouse eye, and the classical resolution limit has not been reached [15,16].

The fully dilated mouse eye has a NA of 0.49, two times greater than that of the human eye. This offers a transverse diffraction-limited resolution 2 times better (0.7 μm *vs*. 1.4 μm, for a wavelength of 550 nm), and an axial resolution limit 4 times better than the human eye (6 μm *vs*. 25 μm). The size of retinal structures is similar in both species, yet the volume of the point spread function (PSF) is 16 times smaller. The larger NA also increases light collection efficiency by fourfold.

To take full advantage of the high NA of the mouse eye, its monochromatic aberrations can be corrected with AO. For confocal imaging, having an improved PSF not only increases image contrast and resolution, but also increases the detected signal. AO has enabled diffraction-limited imaging of cellular and sub-cellular structures in living human and primate eyes [17–22]. Recent studies have also demonstrated benefits of AO applied to rodent eyes [23–25].

In vivo imaging of the mouse eye is challenging due to its small pupil size, large average refractive error, and a retina that is over 50 times thicker than the human retina as measured in diopters, as shown in Table 1. If a deformable mirror is used to section the retina, a much larger stroke is needed for the mouse eye than the human eye.

The small pupil size forces tighter tolerances in designing and aligning an optical instrument and the animal. Given the large focusing range required to cover the mouse retina, the mouse AOSLO has to perform well over a vergence range 5 times larger than that of the human retina (Table 1) [21]. Therefore, the monochromatic aberrations of the AOSLO were minimized over a range of vergences spanning the whole thickness of the mouse retina, as discussed in the next section. In our system, the wavefront sensing source was focused on

#160500 - $15.00 USD Received 3 Jan 2012; revised 13 Feb 2012; accepted 14 Feb 2012; published 15 Mar 2012
(C) 2012 OSA

Table 1. Comparison of the mouse eye and human eye optics parameters*

	Dilated pupil size (mm)	f (mm)	Total eye power	Average refractive error	Average retinal thickness (mm)	Power needed to section the retina	P-V Zernike defocus needed to section the retina**
Human	8.0	16.7	60 D	~0 to +1 D [26,27]	0.25	0.7 D	5.5 µm
Mouse	2.0	1.9	520 D	+7 to +15 D [16,28,29] −7 to −11 D [15]	0.22	49.5 D	25 µm

*Mouse eye focal length in air (f), total eye power and average retinal thickness are calculated from average data for 100 days old C57BL/6 mice [28]. Human eye optics parameters are taken from the Gullstrand-LeGrand Eye Model [30].
**P-V: peak-to-valley.

the outer retina (the most reflective layer), and the reflectance and fluorescence imaging sources were focused on the retinal layer of interest. Monochromatic aberrations affecting the image quality in the planes conjugate to the pupil were also compensated for, in order to achieve good AO correction.

2. Methods

2.1. The fluorescence AOSLO customized for the mouse eye

A custom fluorescence AOSLO was built, combining wavefront sensing methodology previously developed for the mouse eye and design principles of broadband AOSLOs for the human eye [15,21]. A schematic layout of the system is shown in Fig. 1. Note that the actual optical system was folded in 3D, and was flattened in Fig. 1 for illustration.

Three light sources were used for wavefront sensing and imaging after being coupled to single mode optical fibers and mounted on translation stages allowing for independent focusing. All source focuses could be adjusted by changing the distance between the source fibers and their collimating lenses. An 843 nm laser diode (LD) from Qphotonics (Ann Arbor, Michigan, USA) was used as the wavefront sensing source. A 789 nm superluminescent diode (SLD) with 11.5 nm bandwidth (InPhenix, Livermore, California, USA) was used as the reflectance imaging light source. An air-cooled Argon laser (CVI Melles Griot, Albuquerque, New Mexico, USA) provided multiple spectral lines between 457 and 514 nm for fluorescence imaging.

The optical path consists of five, 4-f, afocal telescope pairs that relay image the eye's pupil onto several system pupil planes. All mirrors are commercially available with protective silver coating. The achromatic lens is a 400 mm effective focal length, 100 mm diameter achromat with broadband anti-reflection coating for 400 to 900 nm (Ross Optical, El Paso, Texas, USA). Note that the flatter side of the achromat faces the eye to minimize spherical aberrations for all angles required to form the imaging raster. The system pupil planes include the deformable mirror for wavefront correction, two scanners for raster scanning of the retina, and the SHWS lenslet array. The deformable mirror used was a large stroke hi-speed DM97 from ALPAO S.A.S. (Biviers, Grenoble, France). The deformable mirror controls both the monochromatic aberrations and focus adjustment, and the mouse is never moved, once it is positioned in the instrument. A resonant scanner (Electro-Optical Products Corp, Glendale, New York USA) line-scanned the retina horizontally at 15 kHz, and a slow galvometric scanner (GSI Group Corp, Massachusetts, USA) scanned the vertical direction at 25.5 Hz, forming a rectangular imaging raster. The wavefront sensor consisted of a lenslet array (Adaptive Optics Associates, Cambridge, Massachusetts, USA) with 7.8 mm focal length and 203 µm lenslet pitch, and a Rolera XR camera from QImaging (Surrey, British Columbia, Canada).

Light from the retina was split by a dichroic mirror into a reflectance channel and a fluorescence channel, before detection using photomultiplier tubes (PMT) H7422-40 and −50

#160500 - $15.00 USD Received 3 Jan 2012; revised 13 Feb 2012; accepted 14 Feb 2012; published 15 Mar 2012
(C) 2012 OSA

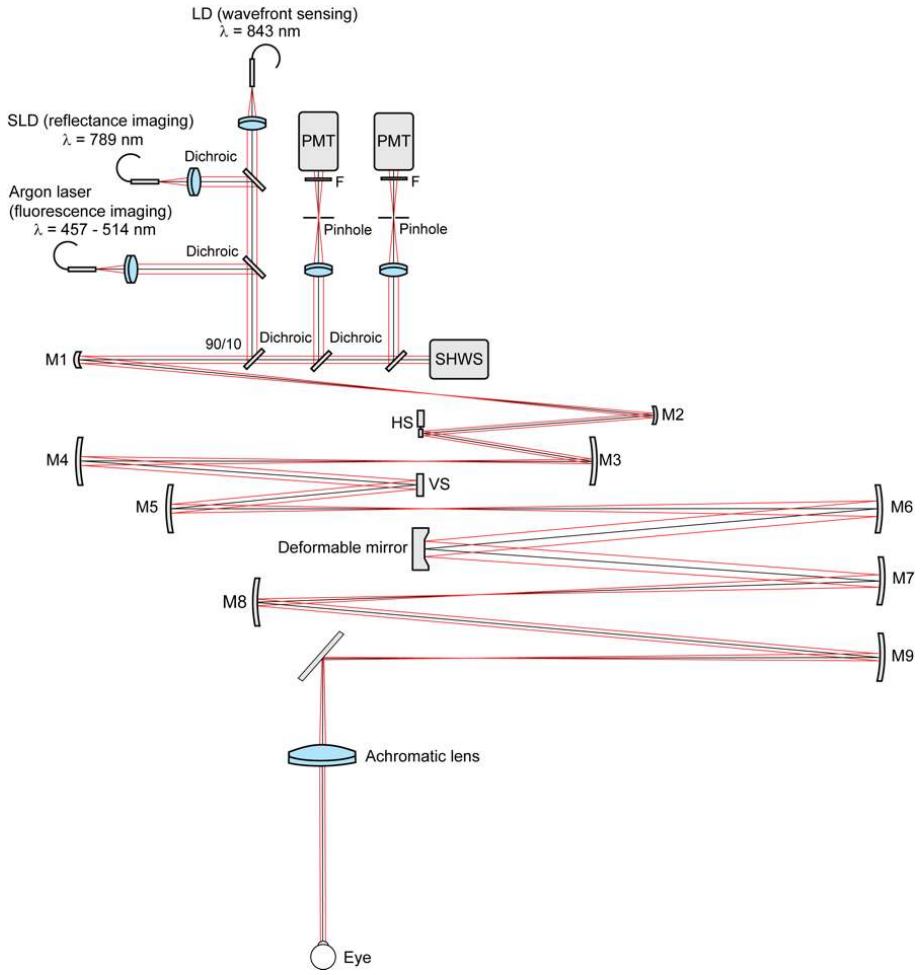

Fig. 1. Schematic of the mouse eye fluorescence AOSLO. LD: fiber coupled laser diode. SLD: fiber coupled Super Luminescent Diode. PMT: photomultiplier tube. SHWS: Shack-Hartmann wavefront sensor. F: band pass filter. 90/10: 90/10 beam splitter. HS: horizontal scanner. VS: vertical scanner. M1-9: Concave spherical mirrors.

from Hamamatsu Corporation (Hamamatsu, Shizuoka-Ken, Japan). The light reaching the PMTs was filtered spectrally by band-pass interferometric filters and spatially by confocal pinholes attached to the front of the PMTs. The confocal pinholes, used on the imaging channel, were between 1 and 3.9 Airy disks in diameter. The PMT output current was amplified and converted to voltage using transimpedance amplifiers (Femto, Berlin, Germany), inverted with in-house electronics, and digitized using a Matrox Odyssey eA framegrabber (Matrox International Corporation, Quebec, Canada).

The first order optical design follows basic design guidelines for a similar instrument built for the human eye [21]. The deformable mirror is placed at the pupil conjugate closest to the eye, to minimize the area used on the optics. The other pupil plane elements are ordered to achieve a gradual change of magnification. Because of the large magnification factor between the deformable mirror plane and the pupil of the eye (approximately 7:1), an additional afocal telescope was added to gradually demagnify the pupil. In order to reduce the astigmatism due to using the spherical mirrors off-axis, spherical mirrors with long focal lengths (ranging from 375 mm to 1000 mm) were selected.

#160500 - $15.00 USD Received 3 Jan 2012; revised 13 Feb 2012; accepted 14 Feb 2012; published 15 Mar 2012
(C) 2012 OSA

Due to the short focal length of the mouse eye, every degree in visual angle subtends only ~31-34 µm on the retina [28], which is an order of magnitude smaller than in the human eye. Therefore, the AOSLO used in for this work was designed to use a small 3° FOV (field of view) with diffraction limited performance, which can be continuously increased up to 10° by changing the scanning angles on both scanners for finding areas of interest. To accommodate a large FOV using all reflective parts, the system performance was heavily driven by the large angle of incidence needed on the spherical mirror closest to the eye, and an achromatic lens had to be used as the last optical element with power to achieve diffraction-limited performance.

After the spherical mirrors were chosen, the only degrees of freedom left were the folding angles or angles of incidence on the spherical mirrors. The optical setup was folded in a non-planar configuration to simultaneously minimize the monochromatic aberrations in retinal and pupil planes [21,31]. The optical layout was designed using CodeV (Optical Research Associates, Pasadena, California, USA) and Zemax (Zemax Development Corporation, Bellevue, Washington, USA). The angles of incidence on the off-axis spherical mirrors were optimized on both the x and y dimensions, under constraints for ray clearance and mechanical mount clearance. The combined optical performance (RMS wavefront error) was optimized on the retinal plane for 9 points uniformly distributed in the scanning field and for three different vergences (–30 D, 0 D, 30 D).

The final system design had diffraction-limited performance for a vergence range of 60 D over a 3° × 3° FOV for high resolution AO imaging. The theoretical system optical performance is shown in Fig. 2 for the shortest wavelength reflected by the spherical mirror coating (450 nm). Note that all spot diagrams were calculated on the focal plane of the mouse eye, assuming a perfect mouse eye and a flat deformable mirror correction. The residual wavefront RMS at 450 nm was lower than λ/20 for all vergences. Because of the mostly reflective nature of the setup, the system performed better for longer wavelengths.

The pupil plane performance was characterized as the image quality for pupil plane re-imaging. This was evaluated along the optical axis over the 3° × 3° scanning FOV, for a wavelength of 450 nm, using the same method as described previously [21]. Figure 3 shows spot diagrams on the 4 pupil planes.

When the optical scanners move to form the imaging raster, if the aberrations are well corrected, the chief ray pivots around a stationary point in the center of the pupil planes. If this is not the case, then the chief ray moves or "wanders" in the pupil plane. This motion blurs the aberrations seen by the SHWS, thus degrading the AO correction. Therefore, we describe the optical performance of the AOSLO in the pupil planes in terms of both the wavefront RMS and the maximum displacement of the chief ray. This beam wander for a 3° × 3° FOV and

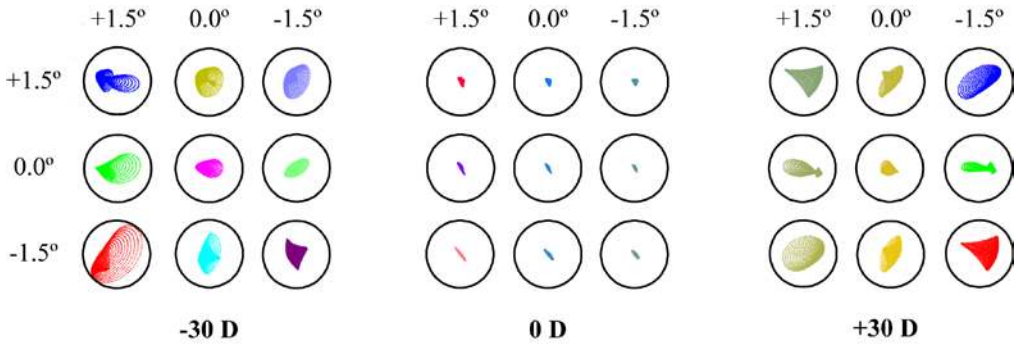

Fig. 2. Spot diagrams for 27 configurations evaluated at the retinal plane, over a 3° × 3° FOV for a vergence range of 60 D in the mouse AOSLO optical design. Configurations are grouped by vergences, and all configurations are diffraction limited for 450 nm of wavelength. The radius of Airy disk (Black circle) is 0.59 µm.

#160500 - $15.00 USD Received 3 Jan 2012; revised 13 Feb 2012; accepted 14 Feb 2012; published 15 Mar 2012
(C) 2012 OSA

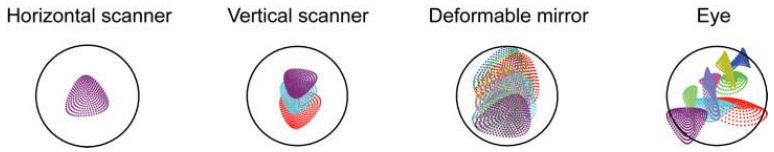

Fig. 3. Spot diagrams for the 4 pupil planes of the mouse AOSLO at 450 nm over a 3° × 3° FOV, for an on-axis point object at the SHWS pupil plane. Different scanning configurations are coded by color. Black circle represents the Airy disk.

60 D of vergence range was ~1% of the pupil diameter (2.0 mm) for a wavelength of 450 nm, and ~4% for a combination of 450 nm, 650 nm and 850 nm light.

For an 8° × 8° FOV, the system is diffraction-limited over a vergence range of 40 D. The wavefront RMS for wavelength of 450 nm is better than are λ/14 for a −22 D to +18 D vergence range. Beam wander at the eye's pupil is ~3% of the pupil diameter for 450 nm light, and ~7% for a combination of wavelengths from 450 nm to 850 nm.

2.2. Adaptive optics

Wave aberrations were measured and corrected at 15 Hz frame rate. Before any source focus compensation and AO correction, the SHWS spots often appear blurry, as shown in Fig. 4(a). When the AO loop is closed, the spots become brighter and sharper, as shown in Fig. 4(b). It typically takes 0.2 seconds (i.e. three iterations) to reach a stable AO correction, with a residual wavefront RMS error at or below 0.05 μm. We always focused the beacon on the photoreceptors to maximize the quality of the SHWS spots. However, we often want to image other planes with light passing through the same deformable mirror. In that case, the change in deformable mirror focus required to image a different layer must be compensated in the wavefront sensing beacon by moving the source fiber tip, so that the beacon stays focused on the photoreceptors. The beacon was refocused by either maximizing subjective sharpness of the SHWS spots, or using a previous calibration done for similar layers.

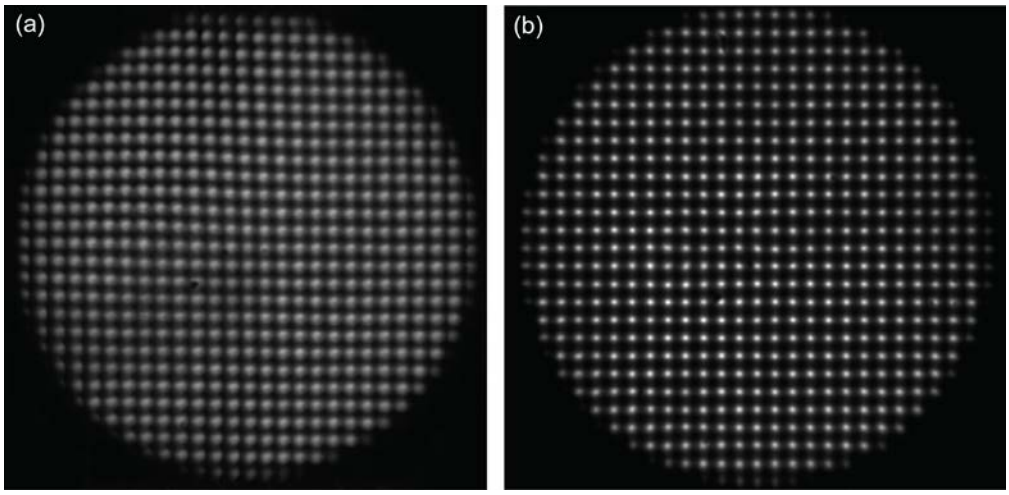

Fig. 4. Typical SHWS spot patterns before the spots are focused on the wavefront sensing source or AO correction (a), and after AO correction (b). The spots are brighter and sharper after AO correction. These SHWS spot patterns are taken at a scanning field of 5° × 5°. Each wavefront sensor spot is sampled by 16 × 16 pixels on the CCD camera. The width of both images is approximately 465 pixels.

2.3. Animals, and preparations for in vivo imaging

Adult wild type mice (C57BL/6J) or transgenic mice (B6.Thy1-YFPH) were imaged [32]. All mice were from 3 to 10 months old and weighed between 20 and 30 grams. Mice were housed

#160500 - $15.00 USD Received 3 Jan 2012; revised 13 Feb 2012; accepted 14 Feb 2012; published 15 Mar 2012
(C) 2012 OSA

in standard mouse cages under 12 hour light/dark cycle. All animals were handled according to the Association for Research in Vision and Ophthalmology Statement for the Use of Animals in Ophthalmic and Vision Research and to the guidelines of the University Committee on Animal Resources at the University of Rochester.

Mice were anesthetized with either Ketamine/Xylazine cocktail injections (100mg/kg and 10mg/kg) only or combined with isofluorane gas (1-2%) and placed on a heating pad prior to *in vivo* imaging. Pupils were dilated with one drop of 2.5% phenylephrine (Neo-Synephrine) and one drop of 0.5% tropicamide. A 0 to +10 D rigid contact lens (Unicon Corporation, Osaka, Japan) with a base curve between 1.55 to 1.70 mm was placed on the eye to maintain corneal hydration during *in vivo* imaging. Mice were stabilized on a bitebar stage with two rotational degrees of freedom as described previously (Bioptigen, Research Triangle Park, North Carolina, USA) [15].

2.4. Power levels, image acquisition and analysis

The maximum permissible light exposure (MPE) for the mouse eye was calculated assuming that the mouse retina possessed the same susceptibility to light damage as the human retina. These calculations included a scaling factor that incorporated the differences in the spot size and retinal illuminance at the mouse retina due to its higher NA. For reflectance imaging, 40 μW and 250 μW were used for the 843 nm laser diode and 789 nm SLD, respectively. Even though the system was to be diffraction-limited for a 3° × 3° high resolution FOV (Figs. 2 and 3), during imaging it was often found that this FOV was too small to cover areas of interest. In reality we often image with a larger FOV (e.g. 5° × 7°), at the cost of slightly larger system aberrations and the FOV is probably outside of the eye's isoplanatic size. The combined powers were less than the MPE for a 20-minute exposure time for a 5° × 7° FOV according to the ANSI guide for the safe use of lasers [33,34]. For fluorescence imaging, cells were imaged using 300 μW of 514 nm laser power measured at the pupil of the eye. This power level, combined with that from the other two sources, is 1.8 times the ANSI MPE for imaging the 5° × 7° FOV for 5 minutes [33,34].

To convert from visual angle to dimensions on the retina, a paraxial model for 100 days old C57BL/6 mice was used [28]. It was calculated that every degree of visual angle corresponds to approximately 34 μm for this model.

To image different layers of the retina using the two channels simultaneously (reflectance and fluorescence), source and detector focuses for both channels were adjusted separately prior to imaging. Sinusoidal frame distortion from the motion of the resonant scanner was compensated by estimating the distortion from imaging a grating target placed in a model eye, and resampling the images using equally spaced pixels. Single *in vivo* fluorescence frames typically possessed very low signal to noise ratio (SNR). Therefore, multiple fluorescence frames were averaged to obtain an image with higher SNR. To account for eye movements between different frames, images were registered using the shifts calculated from simultaneously acquired reflectance images [35].

2.5. Labeling of ganglion cells, in vivo ganglion cell classification, and ex vivo confocal imaging

Ganglion cells were fluorescently labeled with yellow fluorescence protein (YFP) by one of two methods. The first was a transgenic mouse line that expresses YFP in a small subset of retinal ganglion cells (B6.Thy1-YFPH). In the second method, retinal ganglion cells in an adult C57BL/6J mouse were sparsely labeled with YFP via transduction from retrograde viral vector (Equine infectious anemia virus carrying YFP gene; Vector courtesy of Drs. Edward M. Callaway and Ali H. Cetin at the Salk Institute of Biological Studies, California, USA).

Image stacks were taken from the somas and dendrites of the sparsely labeled ganglion cells for classification. Typical image stacks contained 10 slices (with 750 frames averaged for each focus), approximately 6 μm apart in depth and were collected in 5 minutes.

#160500 - $15.00 USD Received 3 Jan 2012; revised 13 Feb 2012; accepted 14 Feb 2012; published 15 Mar 2012
(C) 2012 OSA

One mouse having retrograde viral vector labeling of ganglion cells was sacrificed after multiple *in vivo* imaging sessions. Retinas were isolated and placed as wholemounts on slides with coverslips and covered in mounting medium (Vectashield; Vector Laboratories, Burlingame, California, USA). To visualize boundaries of inner plexiform layer (IPL), cell nuclei in both the ganglion cell layer and the inner nuclear layer were labeled with DAPI overnight. Wholemount images were acquired using a confocal microscope (Olympus FV1000; Olympus, Center Valley, Philadelphia, USA). Image stacks were taken at the same locations as the *in vivo* images using a 40X (1.3 NA) oil immersion microscope objective, and maximum intensity projection images were generated for each stack.

3. Results and discussion

3.1. Imaging of nerve fiber bundles

The innermost surface of the retina contains the nerve fiber layer (NFL) and blood vessels. As shown in Figs. 5 and 6, individual nerve fiber bundles, blood vessels and capillaries were

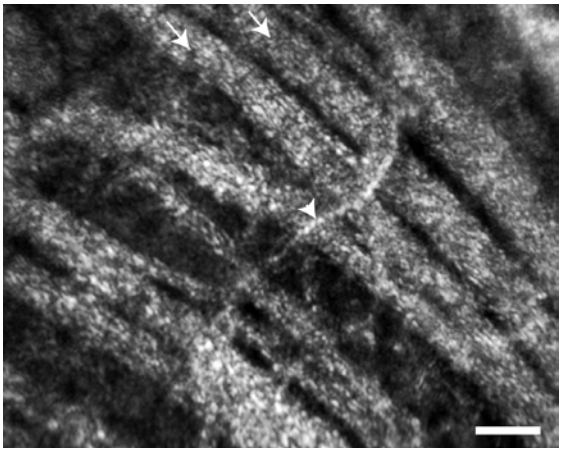

Fig. 5. *In vivo* reflectance image of the NFL close to the optic disk in the mouse eye. This image was an average of 100 frames. Confocal pinhole diameter was 2.1 Airy disks. Arrows: examples of nerve fiber bundles. Arrowhead: example of capillaries. Image was contrast stretched for display purposes. Scale bar: 20 μm.

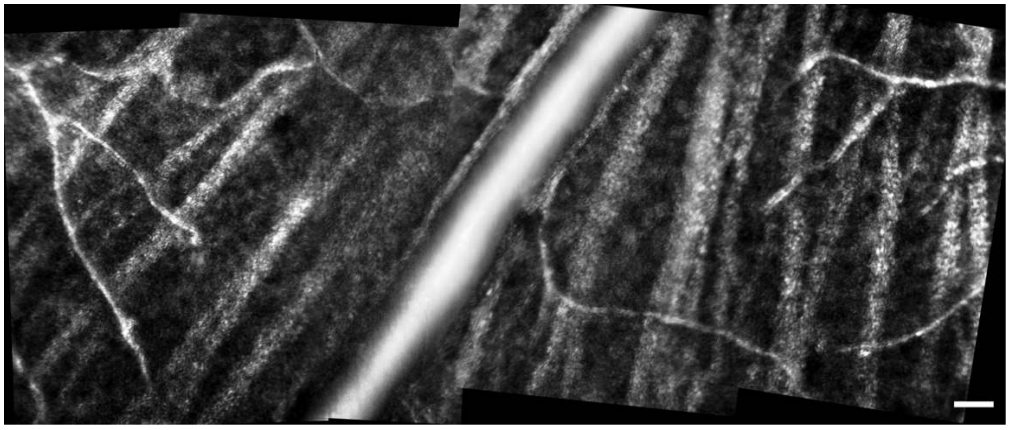

Fig. 6. *In vivo* reflectance image montage of the NFL in the mouse eye, showing a large blood vessel in the center, capillaries, and nerve fiber bundles. This location was over 15 degrees away from the optic disk. Size of this image was 553 μm × 230 μm, or 16.3° × 6.8°. Each individual image was an average of 50 frames. Confocal pinhole diameter was 2.1 Airy disks. Scale bar: 20 μm. Image was contrast stretched for display purposes only.

#160500 - $15.00 USD Received 3 Jan 2012; revised 13 Feb 2012; accepted 14 Feb 2012; published 15 Mar 2012
(C) 2012 OSA

resolved in this layer. Note that the nerve fiber bundles were sparser in Fig. 6 because the retinal location imaged was farther away from the optic disk. Microscopic structures shown as bright white dots could be seen on the nerve fiber bundles, similar to what Dubra *et al.* recently observed in human subjects and postulated that they may be ganglion cell axonal varicosities (unpublished observations) [36]. In between the nerve fiber bundles, some hints of dark "holes" could be seen, with diameters on the order of 5-20 µm. We speculate that these dark "holes" may be ganglion cells.

3.2. Imaging of blood vessels

The supplemental video (Media 1) shows an image stack 135 µm thick, starting at the NFL and moving towards the photoreceptors. Other than the layer of blood vessels and capillaries seen in the NFL, at least two more layers of blood vessels/capillaries were visualized in the mouse retina, corresponding to the three layers of microvessels found in histology (in the ganglion cell layer, inner plexiform layer (IPL), and outer plexiform layer) [37,38]. In this video, the focus depths of the two layers were 68 and 116 µm sclerad from the best focus for the NFL, respectively. Another example of the two capillary layers is shown as averaged images in Figs. 7(b) and (a). The contrast of the capillaries can be enhanced by computing the standard deviation of each pixel throughout the series of registered frames [39,40]. Figure 7(c) shows the standard deviation image corresponding to Fig. 7(a). There were unknown

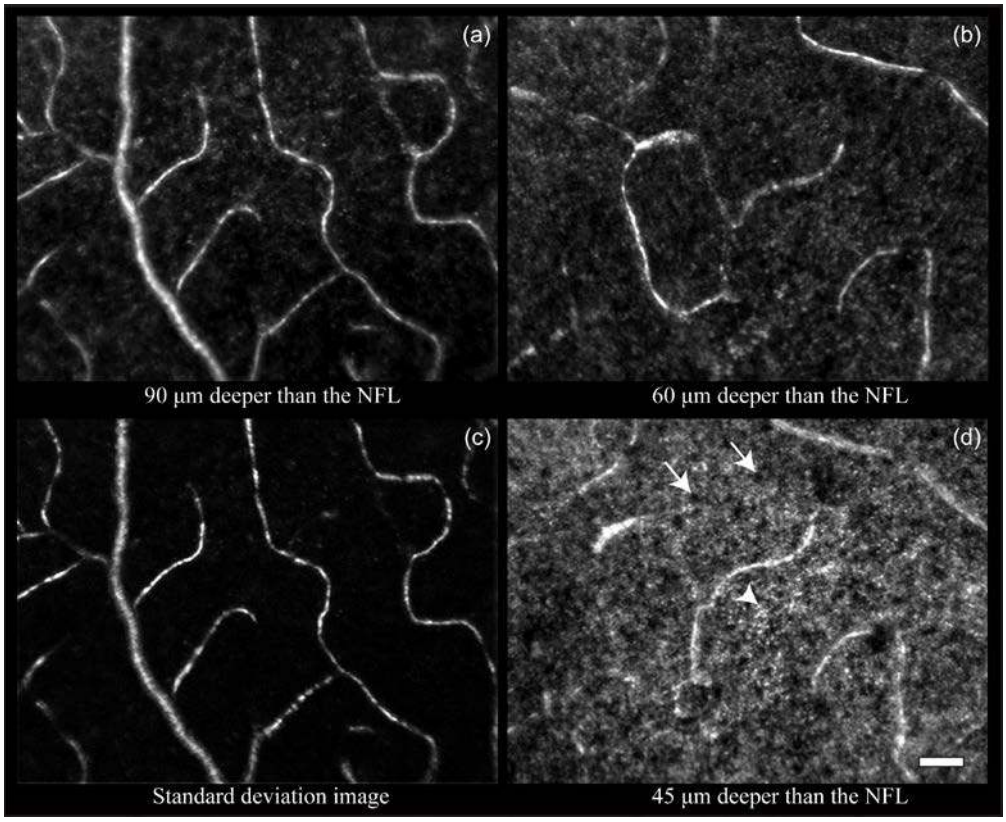

Fig. 7. *In vivo* reflectance capillary images in the mouse retina. All images are taken at the same retinal location. (a), (b), (d) Capillary images at different depths. Each image is a registered average of 50 individual frames. (c) Standard deviation/motion contrast image corresponding to the depth of image (a). Arrows and arrowhead: dark regions and microscopic bright point structures within the intermediate capillary layer. Confocal pinhole diameter was 2.1 Airy disks. All images were contrast stretched identically for display purposes. Scale bar: 20 µm.

#160500 - $15.00 USD Received 3 Jan 2012; revised 13 Feb 2012; accepted 14 Feb 2012; published 15 Mar 2012
(C) 2012 OSA

stationary structures on the capillary layers, which appear as very small bright points and dark holes. This can be seen especially in Fig. 7(d), at an axial focus ~45 µm deeper than the NFL, which was probably in the IPL. The bright spots (arrowhead) may be related to fine processes of ganglion cells and amacrine cells in the inner nuclear layer. There are subtle dark regions between the bright spots (arrows) with spacing between 6 µm to 10 µm, consistent with *ex vivo* estimates of Müller cell spacing at 8.5 µm [41], however positive identification of these structures has yet to be established.

With the axial resolution afforded by the mouse eye's high NA, capillary layers separated by 30 µm can be clearly resolved with no visible cross talk between Figs. 7(a) and (b). At the best focuses for capillaries, motion contrast enhancement [39,40] did not increase the image contrast significantly. Motion contrast can help to increase blood vessel contrast for focus positions such as Fig. 7(d), and can also highlight functional changes such as hemostasis events [42]. Different analyses can be done using the high quality *in vivo* imaging videos (Media 1), including blood vessel diameter, blood flow velocity/blood cells tracking, and 3 dimensional reconstructions of the inner retina. Methods developed for monitoring both the morphology and function of capillaries in human and primates can all potentially be used on the mouse [42–45].

3.3. Imaging of photoreceptors

Due to the small spacing of the mouse photoreceptors, it has not been possible in previous studies to image the complete mosaic in the living eye. With the AOSLO, the photoreceptor mosaic in a live mouse can be imaged non-invasively, as shown in Fig. 8(a). The photoreceptor mosaic was imaged in reflectance, possibly showing both rods and cones. Mouse photoreceptors spacing shows very small variation with retinal eccentricity, less than 40% for cones, and less than 20% for rods [41]. *Ex vivo* data assuming triangular packing indicates average nearest neighbor distances of 1.63 µm for rods and 1.60 µm for rods and cones combined [41]. The concentration of energy in the mosaic spectrum in Fig. 8(b) had a radius corresponding to that predicted from histological observations (1.60 µm), confirming that the observed pattern represents the structure of photoreceptors. The partial circle in Fig. 8(b) indicates the spatial frequency calculated using a 1.60 µm nearest neighbor distance, in agreement with the spectrum of the *in vivo* image.

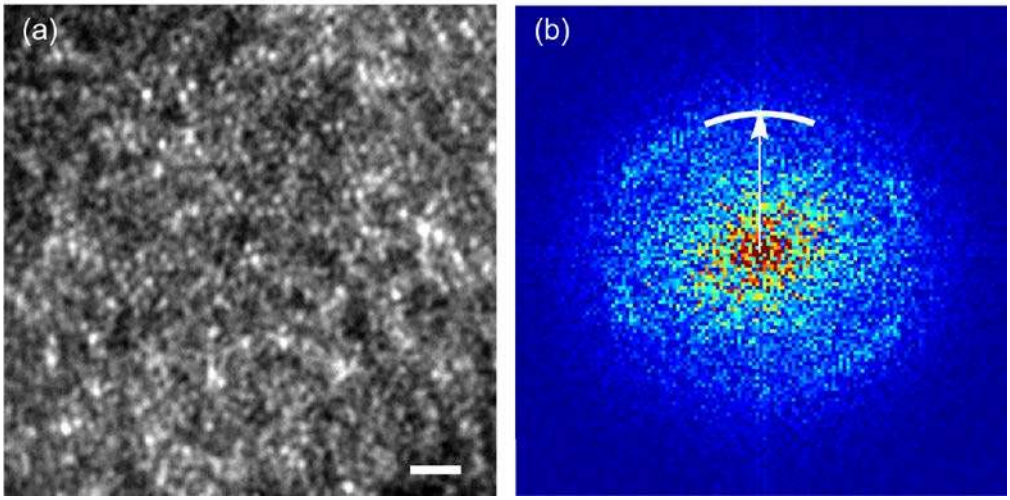

Fig. 8. (a) Photoreceptors imaged in reflectance in the mouse eye. This image is an average of 120 frames. Scale bar: 10 µm. (b) Fourier spectrum of the photoreceptor image in (a), showing a concentration of energy at a fixed radius from the origin. The partial circle indicates the spatial frequency calculated using a 1.60 µm nearest neighbor distance. Confocal pinhole diameter was 2.1 Airy disks. Image (a) was contrast stretched for display purposes.

#160500 - $15.00 USD Received 3 Jan 2012; revised 13 Feb 2012; accepted 14 Feb 2012; published 15 Mar 2012
(C) 2012 OSA

3.4. Fluorescence imaging of subcellular features of retinal ganglion cells

In vivo fluorescence imaging of ganglion cells has been previously demonstrated, allowing the detection of cell drop out [9,46,47]. More recently, axons and dendrites have been resolved in retinas with sparsely labeled ganglion cells *in vivo* [12,14]. Using the same transgenic mouse line, we were able to image individual ganglion cells and processes with much finer resolution than previous studies. The increased axial resolution afforded by AO has allowed us to optically section the cell *in vivo*.

Individual ganglion cells expressing YFP were imaged with the AOSLO, using 514 nm as excitation wavelength. Fluorescence was collected using an interference filter with 534 nm central wavelength and 38 nm bandwidth. After image registration and averaging, the fine details of retinal ganglion cells were resolved. Figures 9(a)-(c) show a ganglion cell imaged at three different focuses, at focus steps of 11.6 μm. At the innermost focus shown in (a), apart from a cell body with its nucleus, two axons were in sharp focus. At an intermediate focus shown in (b), the axons were out of focus and the proximal dendrites of the cell started to come into focus. Finally at the outermost focus shown in (c), the axons were almost completely out of focus and the dendritic field was sharply in focus. Figure 9(d) shows a maximum intensity projection image generated from (a)-(c) and another two intermediate focus images.

Using large blood vessels as landmarks, we were able to follow the same ganglion cells over time. Figure 10 shows another ganglion cell imaged on two different sessions one month apart. Both images were taken using the same power levels and confocal pinhole sizes, and the same fine processes can be resolved over time. The first image was taken with a combined power level at 1.8 times the ANSI MPE (scaled down for the mouse eye as described in the

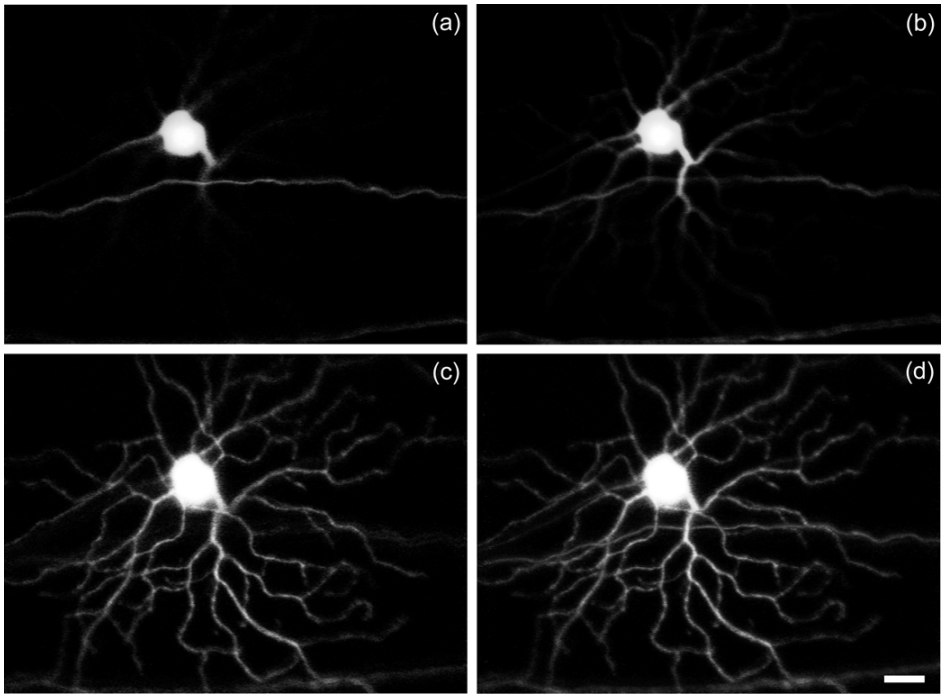

Fig. 9. *In vivo* fluoresence images of a ganglion cell expressing YFP. (a-c) Individual images from three of the focuses, at focus steps of 11.6 μm. Each image at an individual focus step was a registered image average of 500 frames. (d) Maximum intensity projection image generated from 5 separate *in vivo* images taken at focus steps of 5.8 μm. Confocal pinhole diameter was 3.9 Airy disks. All images were contrast stretched identically to preserve their relative brightness. Scale bar: 20 μm.

#160500 - $15.00 USD Received 3 Jan 2012; revised 13 Feb 2012; accepted 14 Feb 2012; published 15 Mar 2012
(C) 2012 OSA

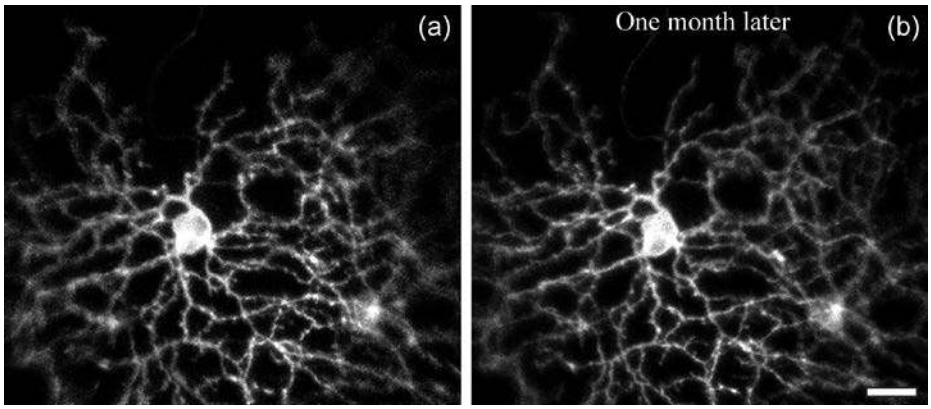

Fig. 10. *In vivo* imaging of the same fluorescent ganglion cells at times separated by one month. Image shown in (a) and (b) are taken one month apart. Both images are maximum intensity projection images generated from 10 separate *in vivo* images at individual focuses. Each image at an individual focus is a registered average of 750 frames. Confocal pinhole diameter was 1.9 Airy disks. Images were contrast stretched identically for display purposes. Scale bar: 20 μm.

Methods section), yet no visible damage could be identified in image stacks spanning the inner retina and the photoreceptor layer in the same location after one month.

3.5. Characterization of in vivo transverse resolution

To estimate the *in vivo* resolution of the imaging system, the transverse cross section across isolated dendrites was measured to be the upper limit of the transverse line spread function (LSF). Note that this resolution characterization was done for the fluorescence imaging channel, and was a conservative estimate. Given that focus adjustment for both the source and confocal pinhole is more difficult for fluorescence imaging than reflectance imaging, resolution for the reflectance channel may be better than what is shown here. Figure 11(a) shows a maximum projection image taken from a focus stack of 7 slices spaced 5.8 μm. The full width half maximum (FWHM) of the transverse cross sections were measured on 9 different locations at their best focuses on the ganglion cell dendritic structure (Fig. 11(b) is shown as an example of a dendrite at its best focus). The measured FWHM of a dendrite cross section was 0.79 μm ± 0.03 μm (mean ± STD) for the 9 locations. In comparison, the theoretical FWHM of the LSF is 0.54 μm (calculated for NA of 0.49, wavelength of 534 nm, and confocal pinhole disk diameter of 1.2 Airy disks). The measured average *in vivo* dendrite cross section was 45% wider than the theoretical LSF. The measurement profile for a typical dendrite cross section labeled by a yellow line in Fig. 11(b) is plotted as an example. In Fig. 11(d), circle data points are the *in vivo* measurement, and solid gray line shows the theoretical LSF.

This *in vivo* dendrite cross section profile represents a convolution of the dendrite profile and the system LSF. In the mouse eye, the diameter of ganglion cell dendrites ranges from 0.7 μm to 1.75 μm as estimated form histology [48]. A rough estimate assuming a dendrite width of 0.70 μm convolved with the theoretical LSF of the system yields a profile (dashed line in Fig. 11(d)) with a FWHM of 0.8 μm, which corresponds very well to the measured *in vivo* FWHM of 0.79 μm ± 0.03 μm. Therefore if the true dendrite diameter is about 0.7 μm at this location, the *in vivo* transverse resolution is near diffraction-limited.

The measured *in vivo* FWHM of 0.79 μm ± 0.03 μm is a conservative estimate of the real system LSF. It would be preferable to measure both the length and diameter of the same dendrite from histology, to confirm that our *in vivo* image scaling from degrees to μm was correct and the actual *in vivo* LSF was near diffraction-limited. Unfortunately histology data for this particular location was not available. However, direct comparison of *in vivo* images to

#160500 - $15.00 USD Received 3 Jan 2012; revised 13 Feb 2012; accepted 14 Feb 2012; published 15 Mar 2012
(C) 2012 OSA

ex vivo histology images at other locations (Figs. 12 and 13) confirmed that our *in vivo* transverse image scaling estimated from paraxial eye model [28] matched very well with *ex vivo* images.

3.6. Characterization of in vivo axial resolution

To estimate the *in vivo* axial resolution of the imaging system, the axial cross section generated by point objects was measured to be the axial point spread function (PSF). These point objects presumably correspond to local concentrations of fluorescence in some ganglion cells. The same focus stack used for transverse resolution characterization was used for this analysis. The theoretical FWHM of the axial PSF is 4.6 μm, and *in vivo* point structures measured in this stack were all sub-resolution compared to the theoretical axial PSF.

The FWHM of the axial cross sections were measured on 6 different locations of the ganglion cell dendritic structure shown in Fig. 11(a). Intensity was measured at the same locations of the image for all focus depths within each focus stack. The measured FWHM of the axial cross section of point objects was 10.8 μm ± 0.7 μm (average ± standard deviation). Axial profile measurement on a typical point object in Fig. 11(c) (arrow) is plotted as an example. In Fig. 11(e), circle data points are the *in vivo* measurement, and solid gray line shows the theoretical PSF. The measured FWHM of the axial cross section of point objects is 2.4 times larger than the theoretical axial PSF FWHM.

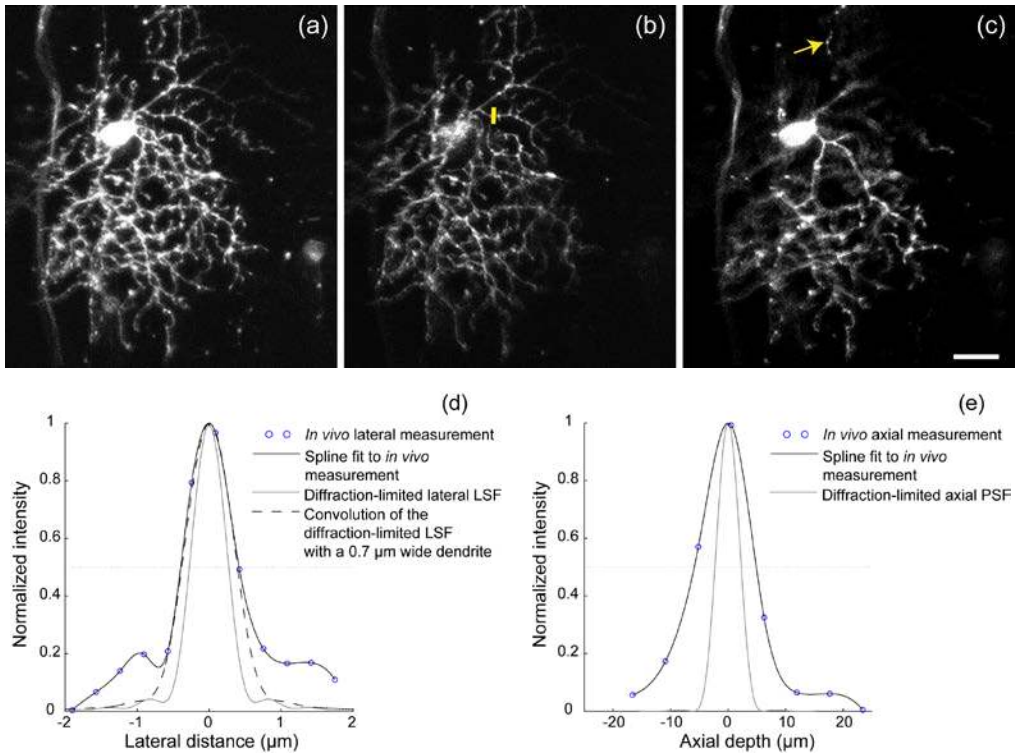

Fig. 11. Characterization of the *in vivo* resolution using an image stack of a fluorescent ganglion cell. (a) Maximum projection image for a focus stack. (b) One individual focus from the focus stack. Transverse cross section on a typical dendrite labeled in yellow is plotted as an example in (d). (c) An individual focus image 11.6 μm shallower than the focus in (b). Arrow indicates measurement position for a typical axial cross section shown in (e). (d) and (e) are the characterization of the *in vivo* transverse and axial resolution, respectively. Circle data points: *in vivo* measurement. Solid black line: spline fit to *in vivo* measurement data. Solid gray line: theoretical diffraction-limited axial PSF. Scale bar: 20 μm.

#160500 - $15.00 USD Received 3 Jan 2012; revised 13 Feb 2012; accepted 14 Feb 2012; published 15 Mar 2012
(C) 2012 OSA

3.7. Characterization of in vivo axial positional accuracy

When imaging objects that are sparsely distributed axially, the axial position of an object or the peak of its axial intensity profile can be localized more accurately than the axial resolution. An axial image stack was equally divided into four image stack segments to characterize the *in vivo* axial positioning accuracy of the mouse AOSLO. Each of the four image stack segments was processed identically. The relative axial positions of 10 different point objects was measured in each of the segments, and the standard deviation of the axial position or the positioning accuracy was 0.36 μm, 30 times smaller than the measured axial FWHM of 10.8 μm. This 30-fold difference is consistent with what was previously reported for an AOSLO developed for the primate eye, which had an axial resolution of 115 μm and a positional accuracy of 4 μm [19].

This fine *in vivo* axial positional accuracy of 0.36 μm has a number of important applications. For example, the stratification of the processes of ganglion cells can be potentially localized to the positional accuracy, enabling classification of ganglion cells *in vivo*.

3.8. Ganglion cell morphological classification, and direct comparison of in vivo to ex vivo images

Ganglion cell morphological classification has been studied extensively using *ex vivo* preparations, and over 14 sub-types have been identified on this basis alone [48–51]. Parameters used for anatomical classification include dendritic pattern (e.g., density of branching), depth of dendrite stratification in IPL, extent of dendritic field, and soma size. While the extent of dendritic field and soma size can be measured using conventional *in vivo* imaging methods, only the AOSLO reported in the current paper can measure the dendritic stratification, and reveal the fine details of dendritic patterning. Being able to classify ganglion cells *in vivo* would create a platform for combining morphological and functional imaging of different cell types in an intact model to study retinal circuitry.

Because we currently don't have an *in vivo* preparation that labels the boundaries of the IPL, we approximated the start of the IPL as the axial position of the proximal dendrites. The

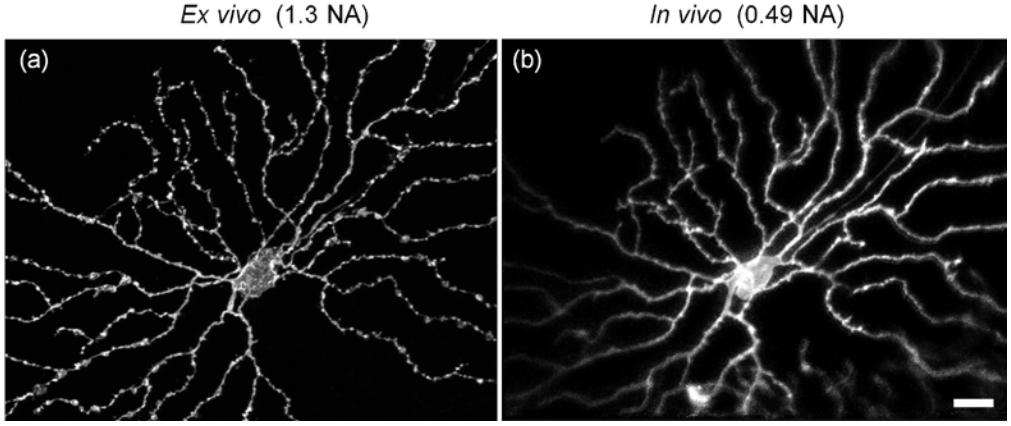

Fig. 12. Direct comparison of *in vivo* and *ex vivo* mouse monostratified ganglion cell. *In vivo* image dimensions (degree to μm conversion calculated using paraxial eye model [28]) matched very well with *ex vivo* image dimensions. (a) *Ex vivo* histological image acquired using a 40x oil immersion confocal microscope with a 1.3 NA objective. (b) *In vivo* image in a mouse retina taken with AO correction over a 0.49 NA. The *in vivo* image was a maximum intensity projection image generated from 11 *in vivo* images taken at different depths. *Ex vivo* image was a maximum intensity projection image generated from an image stack of 51 images. Confocal pinhole size was 1 Airy disk for *ex vivo*, and 1.9 Airy disks for *in vivo* imaging. Scale bar: 20 μm.

#160500 - $15.00 USD Received 3 Jan 2012; revised 13 Feb 2012; accepted 14 Feb 2012; published 15 Mar 2012
(C) 2012 OSA

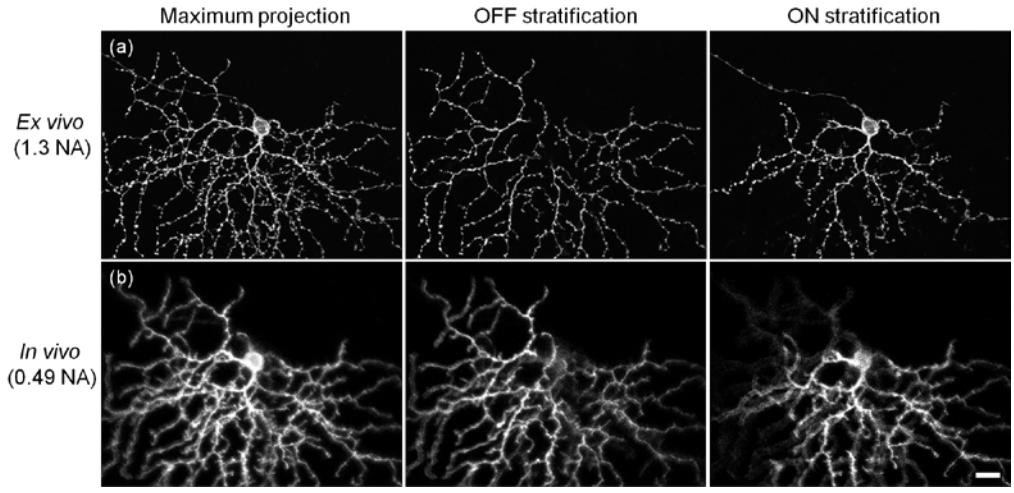

Fig. 13. Direct comparison of *in vivo* and *ex vivo* mouse bistratified ganglion cells. All imaging parameters used were the same as that used for the cell imaged in Fig. 12.

total depth of the mouse eye IPL was approximated to be 35 µm, as measured from *ex vivo* data published by Haverkamp and Wassle [52]. Parameters measured in this work for each cell are: depth of dendritic stratification, dendritic field size and soma size. To estimate dendritic field size for cells with large dendritic field, low-resolution images with large 7° × 9.3° (~230 µm × 300 µm) FOV were taken.

Both monostratified ganglion cells and bistratified cells were identified through *in vivo* imaging. Ganglion cell structures and depth of dendritic stratification measured *in vivo* were directly compared to that measured *ex vivo* in the same retinal locations. Figure 12 shows a monostratified ganglion cell under comparison. Despite that *in vivo* imaging NA was much smaller than that of *ex vivo* confocal imaging (0.49 vs. 1.3), almost all the fine details of the ganglion cell dendrites and axon seen *ex vivo* were also resolved *in vivo*. This cell stratified into the ON sublaminae [48,49]. Despite that different methods were used to identify the

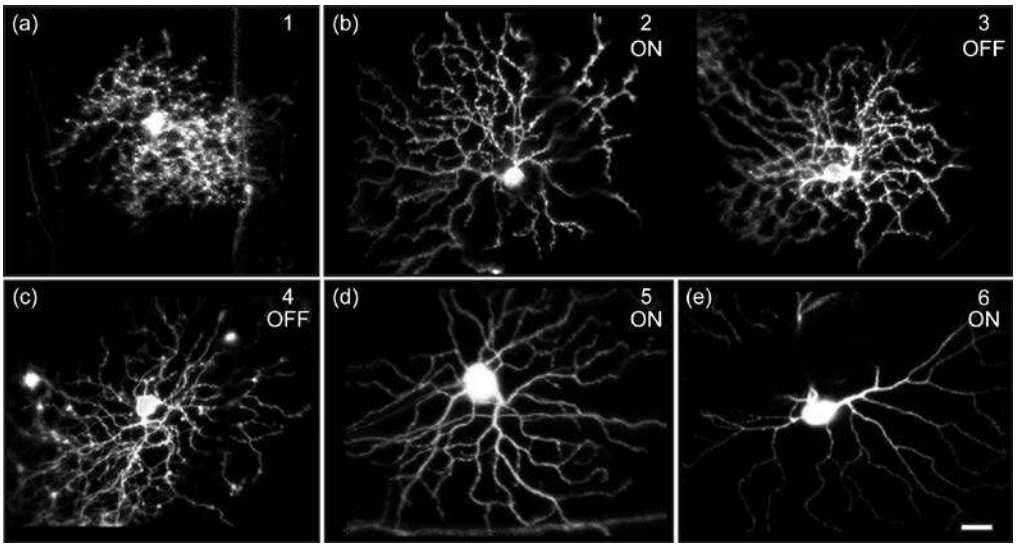

Fig. 14. *In vivo* imaging of six more monostratified ganglion cells. Shadows from large blood vessels can be seen in images of cell 2, 4 and 6. Cells 5 and 6 are taken from transgenic mice with ganglion cells expressing YFP, and all other cells are labeled with retrograde viral vector. Images are contrast stretched for display purposes. Scale bar: 20 µm.

#160500 - $15.00 USD Received 3 Jan 2012; revised 13 Feb 2012; accepted 14 Feb 2012; published 15 Mar 2012
(C) 2012 OSA

boundaries of the IPL for *in vivo* vs. *ex vivo* measurements, the measured dendritic stratification within the IPL showed good agreement. The average depth of dendrite stratification measured *in vivo* was 29% of the estimated total IPL thickness, matching very well with *ex vivo* measurement of 28%. Figure 13 shows a bistratified ganglion cell imaged both *ex vivo* and *in vivo*. Two layers of dendrites separated by ~35% of the IPL or 12 µm could be resolved. The average depth of the dendrite stratification was 49% and 84% as measured *in vivo*, and was 45% and 80% as measured *ex vivo*.

Figure 14 shows six more monostratified cells imaged *in vivo*, and Fig. 15 shows three more bistratified cell examples. Tables 2 and 3 summarize their depth of dendritic stratification measured *in vivo*, and the proposed matching ganglion cell types in the literature. As was described previously, apart from dendritic stratification, dendritic field size and soma size were also measured from *in vivo* images and were used to match cell types (not shown in tables).

Table 2. *In vivo* classification of a few monostratified ganglion cells

	In vivo	**Matching cell types and their dendrite stratification**		
	Dendritic stratification	**Coombs et al.** [48]	**Sun et al.** [49]	**Kong et al.** [51]
Cell 1	65%	M1	RG_{B2}, 67% ± 16%	
Cell 2	44%	M2		1, 55%
Cell 3	88%		RG_{B4}, 66% ± 12%	
Cell 4	72%	M3		3, 73%
Cell 5	47%	M7	RG_{A2} inner, 29% ± 7%	5, 26%
Cell 6	30%	M8		
Cell from Fig. 12	28%			

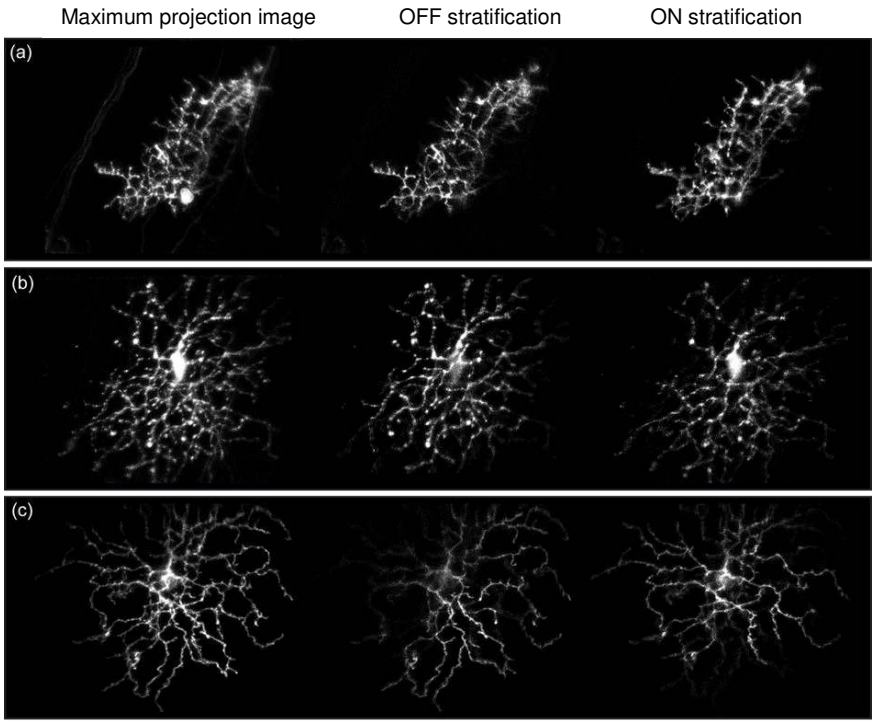

Fig. 15. *In vivo* imaging of three more bistratified ganglion cells. The left column shows the maximum projection image of the cell; middle and right columns shows the dendrite stratifications at 2 different focuses. All images are contrast stretched for display purposes. Scale bar: 20 µm.

#160500 - $15.00 USD Received 3 Jan 2012; revised 13 Feb 2012; accepted 14 Feb 2012; published 15 Mar 2012
(C) 2012 OSA

Table 3. Summary of *in vivo* classification of a few bistratified ganglion cells

	In vivo	Matching cell types	
	Dendritic stratification	**Coombs et al.** [48]	**Sun et al.** [49]
Cell a	49% and 72%	M11	RG_{D1}, 44% ± 8% and 71% ± 8%
Cell b	42% and 78%	M13	RG_{D2}, 39% ± 10% and 71% ± 12%
Cell c	56% and 96%	M14	
Cell from Fig. 13	49% and 84%		

4. Conclusions and future directions

In vivo imaging of the mouse eye can provide higher transverse and axial resolution than of the human eye, despite challenges encountered in previous studies [23,24]. We have constructed a confocal scanning AO instrument with a wavefront sensor operating on back-scattered light, providing a fast and effective correction of mouse eye aberrations. The imaging part of the instrument was custom designed for the mouse eye to provide diffraction-limited optical performance over a 60 D vergence range, and low beam wander on the eye's pupil plane. After AO correction, the photoreceptor mosaic, nerve fiber bundles, fine capillaries and blood flow were visualized *in vivo* non-invasively in reflectance. Ganglion cell bodies, dendrites and axons were clearly resolved in registered *in vivo* fluorescent images.

Compared to a previous system we modified for AO imaging in the rat eye [25], this system was purposely built for the mouse eye, utilizing the eye's full NA and delivering images with higher resolution and contrast. Imaging resolution characterized directly from *in vivo* images was sub-micron laterally, and ~10 μm axially.

We report the first *in vivo* images of the photoreceptor mosaic in mice. The ability to identify ganglion cell types based on the plane of stratification indicates the unprecedented *in vivo* axial resolution.

Together with current powerful molecular techniques that exist for engineering the mouse, this high resolution *in vivo* method opens new doors for many investigations and experiments. AO imaging of mouse models has potential for investigating retinal development, disease mechanisms and evaluating the efficacy of drug therapies. For example, capillary morphology and blood flow can be studied longitudinally for mouse models of vasculature diseases such as diabetic retinopathy. For mouse models of glaucoma, ganglion cells and their processes as well as microscopic structures in the nerve fiber layer can be monitored during disease progression or treatment. With the fine *in vivo* axial positional accuracy reported here (0.36 μm), the axial movement of small isolated features or processes could potentially be finely tracked for their response to light or over the visual cycle, or a longer time scale for retinal development or disease progression.

While we have concentrated on reflective structures and fluorescently labeled ganglion cells in this study, the observed resolution indicates that it is possible to use the fAOSLO to image a variety of other retinal structures. These include individual pericytes, Müller glial cells, bipolar cells and amacrine cells that are fluorescently labeled in transgenic mice [53,54], or using cell-specific adeno-associated virus (AAV) and lentiviral vectors [55–58]. Also included are autofluorescent retinal pigment epithelium cells that may be resolved without using extrinsic fluorophores [59].

Other than imaging morphology, the mouse AOSLO may also provide measures of retinal function at a cellular and subcellular scale. Combining AOSLO imaging with recent advancement in optogenetics, it will be possible to study and manipulate retina circuitry in an intact retina. Using genetically encoded calcium indicators, we have started to record the light response of ensembles of ganglion cells in the living mouse eye [60]. We have also started probing the function of pericytes in regulating capillary blood flow [61]. Furthermore, this instrument can be used to image and probe other retinal cells that are presynaptic to ganglion cells, such as bipolar cells and amacrine cells. In the future, we could capitalize on transgenic mouse lines with sub-type specific markers for ganglion cells or other retinal cell types

#160500 - $15.00 USD Received 3 Jan 2012; revised 13 Feb 2012; accepted 14 Feb 2012; published 15 Mar 2012
(C) 2012 OSA

[62,63], and study function for each particular sub-type. Eventually this technique may allow us to characterize retinal circuitry by optically monitoring the electrical activity of large numbers of interconnected neurons simultaneously.

The current system operates as a confocal AOSLO, and needs a confocal pinhole to achieve axial sectioning. Two-photon imaging is a method to achieve intrinsic axial resolution by preferentially exciting fluorophores near the focal volume, thus reducing photobleaching [64]. Adaptive optics two-photon imaging has been demonstrated for imaging photoreceptors in the living primate eye [65], and we expect an increase in two-photon signal intensity in a mouse eye with larger NA. Modifying a confocal mouse AOSLO to accommodate two-photon imaging involves the addition of an ultrafast pulsed laser, and a channel for direct detection of two-photon fluorescence by-passing the de-scanning optics used for confocal detection [66]. For functional imaging using extrinsic fluorophores, such as optical recording of ganglion cells, it allows imaging with an IR wavelength outside of the retina's sensitivity range, avoiding intense stimulation caused by single-photon fluorescence imaging. Two-photon imaging also permits excitation of multiple endogenous fluorophores, such as NADH, that are functional markers of cell metabolism. All kinds of transparent retinal structures contain two-photon excitable intrinsic fluorophores, and can be imaged with high contrast on a two-photon microscope *ex vivo*. If enough signal intensity can be collected in the mouse eye using AO two-photon imaging, potentially both the morphology and function of any retinal cell types may be monitored *in vivo* without the use of exogenous fluorophores.

Acknowledgments

We appreciate financial support from the following sources: NIH Grants EY 001319, EY014375, EY018606, EY021166, NSF STC grant No. AST-9876783, and Research to Prevent Blindness. Alfredo Dubra-Suarez, Ph.D., holds a Career Award at the Scientific Interface from the Burroughs Wellcome Fund. Richard T. Libby holds a Research to Prevent Blindness Career Development Award. We are grateful to Edward Callaway and Ali Cetin for providing viral vector for retrograde labeling of ganglion cells. We also thank Wanli Chi, Jesse Schallek, Benjamin Masella, Jennifer Hunter, Jason Porter, Boshen Gao, Jannick Rolland, Kevin Thompson, Julie Bentley, Stephen Burns, Frederic Rooms and Ram Kumar Sabesan for their assistance on this work, and Jennifer Strazzeri for assistance with intracranial injection of viral vector. We would also like to thank the reviewers for providing valuable comments and suggestions for the manuscript.

#160500 - $15.00 USD Received 3 Jan 2012; revised 13 Feb 2012; accepted 14 Feb 2012; published 15 Mar 2012
(C) 2012 OSA